Journal of Magnetic Resonance Open 23 (2025) 100194

Contents lists available at ScienceDirect

Journal of Magnetic Resonance Open

journal homepage: www.sciencedirect.com/journal/journal-of-magnetic-resonance-open

Robotic arms for hyperpolarization-enhanced NMR

Kirill Sheberstov [a,1,*], Erik Van Dyke [b,c,d,1], Jingyan Xu [b,c,d], Raphael Kircher [b,c,d], Liubov Chuchkova [b,c,d], Yinan Hu [e], Sulaiman Alvi [f], Dmitry Budker [b,c,d,f], Danila A. Barskiy [b,c,d,*]

[a] Laboratoire des biomolécules, LBM, Département de chimie, École normale supérieure, PSL University, Sorbonne Université, CNRS, 75005, Paris, France
[b] Institut für Physik, Johannes Gutenberg-Universität Mainz, 55128, Mainz, Germany
[c] Helmholtz Institute Mainz, 55099, Mainz, Germany
[d] GSI Helmholtzzentrum für Schwerionenforschung GmbH, 64291, Darmstadt, Germany
[e] State Key Laboratory of Brain and Cognitive Science, Institute of Biophysics, Chinese Academy of Sciences, Beijing, 100101, China
[f] Department of Physics, University of California, Berkeley, CA, 94720-7300, USA

ARTICLE INFO

Keywords:
NMR
Robotic arm
Low field
Hyperpolarization
Photo-CIDNP
PHIP
SABRE

ABSTRACT

Optimization of nuclear spin hyperpolarization experiments often require varying one system parameter at a time (or several parameters in a nontrivial manner) as well as multiple repetitions of signal measurements. Use of automated robotic systems can significantly streamline this optimization process, accelerating data acquisition and improving reproducibility in the long term. In this work we show an exemplary system built on open-source components and demonstrate several benchtop and ultralow-field NMR experiments employing photo-CIDNP and SABRE-derived hyperpolarization. This work illustrates that open-source platforms employing benchtop NMR and robotic systems built in a modular manner with remote operation allow the implementation of various unconventional experiments in a reproducible manner.

1. Introduction

In this brief article we discuss the use of automated robotic arm systems in a university-based nuclear magnetic resonance (NMR) laboratory specializing in benchtop and zero- to ultralow-field (ZULF) experiments. We motivate our discussion by recalling the origins of the discoveries of hyperpolarization techniques, which in recent decades have been broadly applied to boost signal intensities in NMR.

Three generic approaches to hyperpolarization are dynamic nuclear polarization (DNP), chemically induced DNP (CIDNP), and parahydrogen-induced polarization (PHIP) [1]. Historically, DNP was discovered first; in this method, polarization of unpaired electrons is transferred to nuclear polarization [2]. CIDNP effects were discovered about 15 years later and were initially attributed to DNP mechanism [3]. The correct mechanism responsible for CIDNP was independently proposed by Closs [4] and Kaptein in 1969 [5,6] and it is based on the concept of a radical pair. Curiously, parahydrogen-induced polarization (PHIP) was also initially misinterpreted: this time, as CIDNP [7]. It took several years to understand that the "Monday morning effect," as it was once called, has something to do with parahydrogen (pH_2) at liquid-N_2 temperatures [8]. Today, DNP-, CIDNP-, and PHIP-based approaches are well understood and are widely used for material characterization, drug screening, and molecular imaging among a diverse range of various applications.

A common thread found in these groundbreaking works is that virtually all of the first hyperpolarization experiments were performed manually, and the greatest discoveries often merely demonstrated effects (or lack of thereof) without reaching high levels of precision. Understanding details and establishing a proper theoretical framework to explain unexpected observations required additional time and effort from many groups. We believe that this remains true to this day. While now the research community can create a variety of automated systems capable of streamlining scientific process, in most instances, the real usefulness of a discovery can be understood only with time. The reproducibility of experiments by different groups is still of central importance to facilitate proper understanding of observed phenomena.

* Corresponding authors at: Laboratoire des biomolécules, LBM, Département de chimie, École normale supérieure, PSL University, Sorbonne Université, CNRS, 75005, Paris, France.
E-mail addresses: kirill.sheberstov@ens.psl.eu (K. Sheberstov), dbarskiy@uni-maiz.de (D.A. Barskiy).
[1] These authors contributed equally.

https://doi.org/10.1016/j.jmro.2025.100194

Available online 3 March 2025

Robotization of the research workflow can significantly accelerate productivity [9–12]. In the context of NMR applications, automation is especially promising in conjunction with hyperpolarization techniques where samples must be physically manipulated [13–23]. One of the most often automated processes in hyperpolarization-enhanced NMR is field cycling which is typically achieved via sample shuttling between different magnetic field regions. Various approaches are used for shuttling, e.g. stepper motors that are reasonably fast and very precise [17,19], flow systems that are simple to implement [22,23], and pneumatic shuttling systems that probably provide the fastest solutions [18,24,25]. Robotic arms have also seen use in shuttling samples and offer unique advantages, such as rapid incorporation in different experiments with fewer restrictions on the spatial arrangements of other components (they are more modular).

In this work, we demonstrate universality of the robotic arm systems for hyperpolarization-enhanced NMR by showcasing photo-CIDNP and SABRE (signal amplification by reversible exchange) [26] experiments conducted on the bench in a variety of magnetic field regimes (from 1.4 T down to zero field). By "systems" we mean combination of robotic arm, hyperpolarization apparatus and the detection apparatus (ZULF NMR or benchtop NMR). Construction of a modular, open-source, easy-to-build setup is described in detail with the goal of making similar systems accessible to the community.

2. Results and discussion

A cartoon of a robotic arm-based system adapted for hyperpolarized NMR experiments using two detection modalities is shown in Fig. 1. The key property of this system is modularity, meaning that it is easy to adjust the configuration in such a way as to perform different types of hyperpolarization routines. In particular, we used the system described in this work to perform measurements described in Refs. [27–31]. When photo-CIDNP was used as a hyperpolarization modality, the robotic arm moved the sample between the polarization region (where light excitation was performed) and the detection region. Detection was performed using either a benchtop NMR spectrometer [27] or ZULF NMR

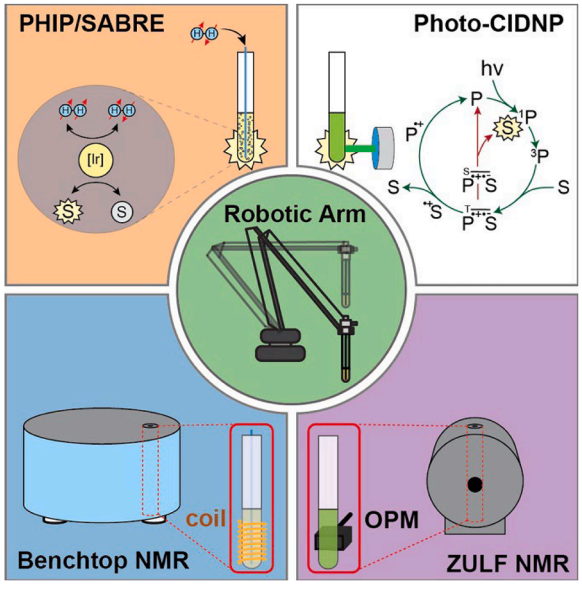

Fig. 1. A robotic arm was used to transfer the sample between hyperpolarization and observation sites. Hyperpolarization was achieved through either PHIP/SABRE or photo-CIDNP (top quadrants), whereas detection was performed either inductively using a benchtop NMR spectrometer or with an optically pumped magnetometer (OPM) in the zero-to-ultralow-field (ZULF) regime. A robotic arm was used as a universal sample transporter to perform magnetic field cycling and to store a sample in the selected field.

apparatus with atomic magnetometer detection [29]. PHIP-relay was also demonstrated using the same modular system [28,31].

In this tutorial paper, we show the technical aspects of the system itself and describe additional results for a PHIP variant, SABRE [26], specifically, low-field signal buildup and relaxometry measurements for pyrazine in methanol.

Various robotic arms are available on the market. **Table S3** presents examples and comparisons in which robotic arms are sorted according to their price. The category with the lowest price of $1000 and below belongs to the so-called "toy" robotic arms, which are used in educational applications. We tried two low-price variants (Tinkerkit Braccio from Arduino and uArm Swift Pro from Ufactory) and found that even though the precision of a plastic robotic arm was insufficient, the quality of a cheap metallic robotic arm equipped with stepper motors (uArm Swift Pro) was high enough for the typical manipulations with NMR tubes described in this work. The precision of motion is crucial because the robotic arm holds the sample at the top, the position of the bottom is not fixed, and is typically 300 mm lower than the top of the long tube. Without additional precautions, the sample can be crushed upon transfer, particularly during operations that include placing the sample in tight spaces such as taking a measurement in a benchtop spectrometer. To circumvent this problem, insertion of the sample inside any device can be facilitated with a 3D-printed cone piece fixed at the entrance of a device with an upper hole of approximately 20 mm and a lower opening of 10 mm, which allows for safe guiding of the NMR tube inside a target location. Robotic arms are typically equipped with special holders that can pick up samples using vacuum caps. We used sample holders available from Magritek attached to the top of the NMR tube that were lifted pneumatically by the arm. This was a convenient solution for photo-CIDNP experiments, in which the sample was free of tubing. In contrast, in the SABRE experiments, the sample had to be pressurized by H_2 gas such that tubing was connected to the top of the sample. Therefore, we used a 3D-printed piece attached rigidly to the robotic arm and NMR tube. We note that some robotic arms are equipped with anti-block grippers that also can be used to hold samples [14].

Table S3 also lists the specifications for more expensive robotic arms with industrial quality. In this work, we have not tested them but they may be good options in applications requiring fast sample transfer and robustness.

2.1. Benchmarking the performance of the robotic arm

With lower-priced devices, it is always a good idea to verify the performance and benchmark them individually. We regularly performed the tests described below to characterize the basic modes of motion and their reproducibility. To do this, the robotic arm is programmed to perform repetitive cycles of motion (up and down or left and right) between two fixed points in space. For every cycle, the total time required for the motion is calculated using a Python script and then saved to a file. Multiple of these tests were performed for the uArm Swift Pro robotic arm over the years of its usage in our lab, and some recent results are shown in Fig. 2. In general, there are two motion regimes available for this robotic arm: slow and fast. A fast mode of motion is achieved by activating only one motor. As a result, the head of the arm moves in an arch trajectory, as shown in Fig. 2A and B with arrows "2" for vertical and "4" for lateral movements, respectively. The alternative mode is when the head moves along a straight line connecting the two points (movements "1" and "3"). However, this motion requires simultaneous activation of two motors and can be up to three times slower. The distance between the starting and ending points was 194 mm (slow) and 234 mm (fast) for vertical motion and an arc of 78° for lateral motion. The timing to complete the movement in a single direction was measured from initiation to completion; an additional delay of 1 s in between each movement was added but not included in the final measurement. We measured the timing required for these types of motion by repeating them 1000 times and plotted the histograms of the time

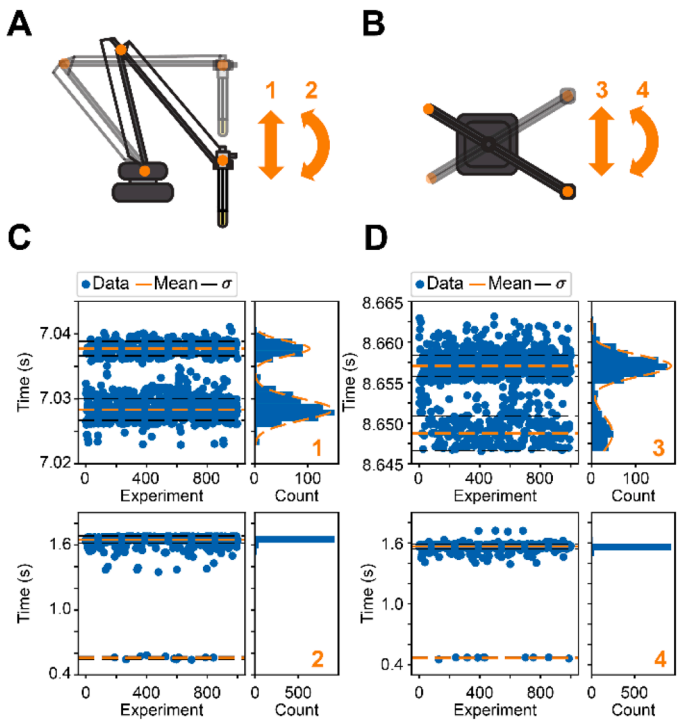

Fig. 2. Schematic view of (A) the vertical movement types and (B) the lateral movement types of the robotic arm used in our laboratory; (C-D) Histogram corresponding to the measurements of time necessary to complete separate movements (indicated by numbers 1–4) with relevant statistical parameters indicated.

distributions in Fig. 2C and D. Most of the time, the timing precision falls within tens of milliseconds, but sometimes outliers are observed. For instance, in the case of "fast" movements, this is especially visible with most movement durations for up and down motion lasting 1.65 ± 0.03 s with outliers consistently appearing around 0.5 s with a narrow distribution (0.557 ± 0.012 s, $N = 12$). Similarly with rapid rotational movement, a distribution around 1.56 ± 0.02 *s* is observed with outliers appearing again around 0.5 s with a narrow distribution (0.468 ± 0.006 s, $N = 10$). This is in contrast to slow movements which require activation of two motors, where we observe the presence of a two-mode distribution with values of 7.028 ± 0.0017 s and 7.038 ± 0.0012 s for vertical motion, and 8.648 ± 0.002 s and 8.657 ± 0.0014 s for rotational movement. We could not resolve this problem by reinitializing the arm each time before motion. Therefore, to avoid outliers in NMR experiments where movements of differing speeds are used, we verified the timing such that the time of motion was always within the required range (± 50 ms) and discarded the spectra in case of failure.

2.2. Photo-CIDNP experiments

The utility of the robotic arm in photo-CIDNP field-cycling experiments is demonstrated in Fig. 3. Here, we emphasize the importance of signal averaging, as the individual NMR signals (Fig. 3B for ^{1}H and Fig. 3E for ^{13}C NMR spectra) have a low signal-to-noise ratio, i.e., the signals in individual ^{13}C NMR spectra are hardly distinguished from the noise. Yet, once combined, spectral features of the hyperpolarized 1,4-benzoquinone isotopomers are clearly visible in both ^{1}H and ^{13}C NMR spectra at 1.4 T (Fig. 3C, F) due to the reproducibility of each separate shuttling experiment.

The physics and methodology of these experiments, along with assignment of the peaks were previously discussed in [27]. The hyperpolarized state in the ZULF regime corresponds to a heteronuclear singlet order formed between ^{1}H and ^{13}C spins in para-benzoquinone. Photo-CIDNP hyperpolarization experiments conducted with the aid of benchtop NMR spectrometers are especially promising for fragment-based drug discovery [32]. Changes in line intensity and relaxation times may report on the presence of the protein–ligand interactions. In typical magnetic fields of benchtop NMR (1–2 T), photo-CIDNP usually hyperpolarizes magnetization. Hyperpolarized heteronuclear long-lived states at μT fields may provide even higher relaxation contrast upon protein-macromolecule binding.

While detecting ^{13}C NMR spectra it was crucial to decouple the protons to remove the line splitting. On the other hand, it was important to leave ^{13}C spins untouched for the detection of ^{1}H NMR spectra, such that signals belonging to different protons would not overlap due to J-couplings. Light irradiation was performed in fields below 0.5 μT to generate hyperpolarization, and after sample transfer (around 7 s), detection was carried out in a benchtop NMR spectrometer. The use of a robotic arm allows one to easily accumulate transients in such experiments. In the considered example, the signal-to-noise ratio in a ^{13}C spectrum is *ca.* 2 for the low-intensity signal. We note that hyperpolarization level in these experiments is substantial (enhancement *ca.* 200 with respect to equilibrium ^{13}C signal at 1.4 T), enabling detection of a 5 mM solution at natural abundance of ^{13}C nuclei with a benchtop NMR spectrometer.

2.3. SABRE experiments

SABRE results employing pyrazine as a substrate, [Ir(IMes)COD]Cl (IMes = 1,3-bis(2,4,6-trimethylphenyl) imidazole-2-ylidene, COD = cyclooctadiene) as a polarization precatalyst, and methanol as a solvent, are shown in Fig. 4. SABRE hyperpolarization at 7 mT builds up smoothly, as shown in Fig. 4A, when detection is carried out with 1 T proton benchtop NMR (Magritek). By fitting the buildup curve with a first-order monoexponential function we determined the build-up time constant to be approx. 8 s. A logarithmic scale in which data points for short (hundreds of ms) pH_2 bubbling durations are well visible is shown at the bottom. Note that polarization buildup at such short bubbling durations does not follow simple monoexponential rising behavior and has an "induction period" likely due to hydrogen dissolution kinetics and dynamics. We also note that the timing reflected in the *x*-axis indicates the length of time that the parahydrogen flow is directed towards the reaction chamber by closing a bypass valve (see the Supplementary Information for a detailed schematic), so there is likely a delay in the parahydrogen supply at short time intervals due to the dynamics of the gas flow.

By varying the waiting time after hyperpolarization at low field, relaxation of the hyperpolarized ^{1}H magnetization in different fields was studied, as shown in Fig. 4B (50 uT) and Fig. 4C (7 mT). When measured with a 1.04 tesla benchtop NMR instrument, the relaxation time constant at Earth's field was approx. 6 times smaller than the one at 7 mT. Moreover, the logarithmic scale of the signal decay at 7 mT (Fig. 4C) shows a clear plateau for short waiting times (<5 s) which is likely caused by the continuation of the SABRE buildup process after nominal cessation of the current to the valve controlling pH_2 flow. Overall, these experiments demonstrate sufficient robustness of an affordable robotic arm system to observe time dependences in question even when sample transfer takes place through regions with varying magnetic fields (i.e., in our case transfer through the Earth's field did not destroy polarization).

We also performed similar SABRE experiments with detection at ultralow magnetic field (2 μT) using a home-built ZULF apparatus (Fig. 5). In this case, hyperpolarization buildup at 7 mT surprisingly revealed a different time constant of approx. 26 s (Fig. 5A). Performing experiments with the same NMR tube and solution on the same day by switching between different detection modalities confirmed that the effective buildup time constants are different (7–8 s when measured with proton benchtop NMR and 23–26 s when measured with atomic magnetometer at ZULF conditions). Moreover, when performing the

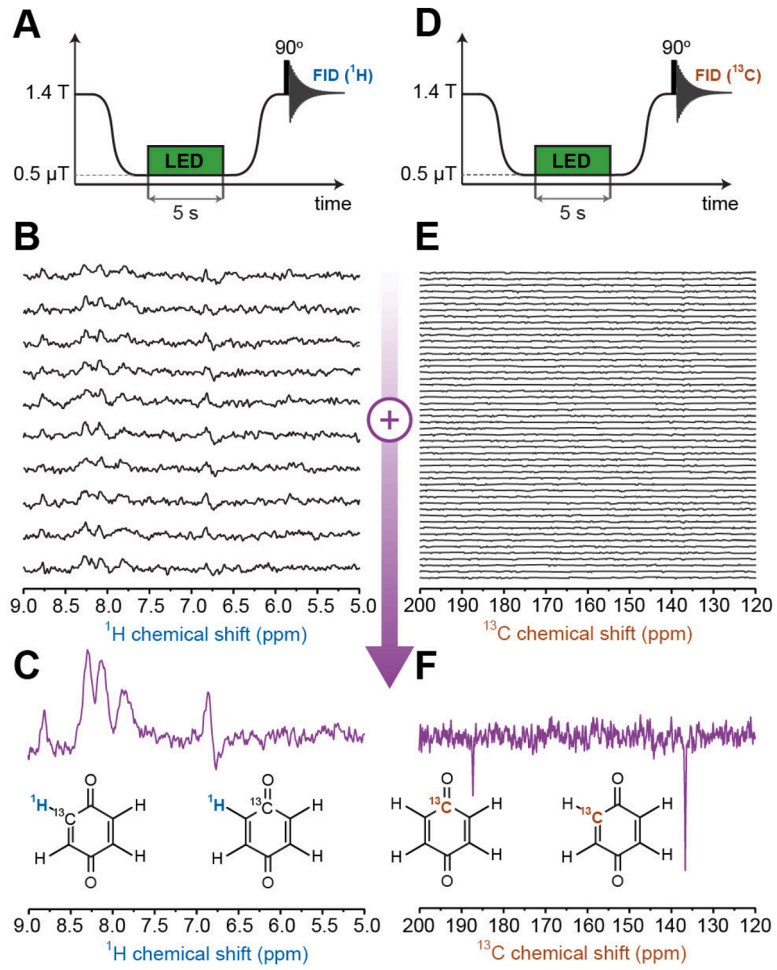

Fig. 3. Photo-CIDNP proton and carbon-13 experiments. (A) and (D) illustrate experimental protocol for a single scan. Note that ^{13}C detection was done with ^{1}H decoupling; LED = light-emitting diode. (B) and (E) show individual spectra; (C) and (F) show summed ^{1}H and ^{13}C spectra respectively.

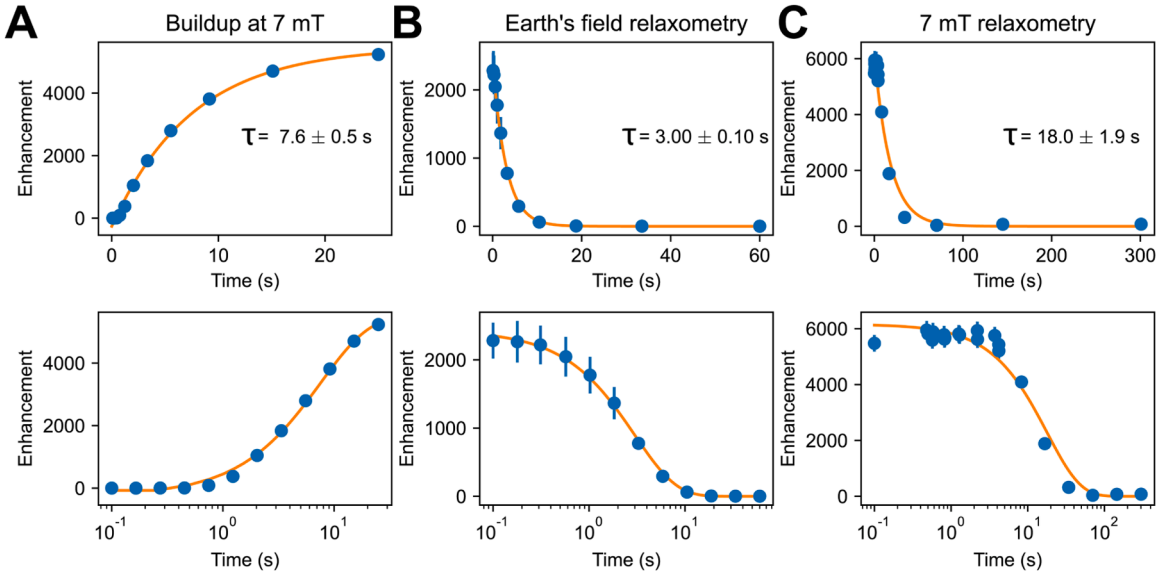

Fig. 4. Proton SABRE-enhanced benchtop NMR measurements conducted using robotic arm system with a sample of pyrazine (60 mM) and SABRE catalyst [Ir(IMes)COD]Cl (3 mM) in methanol using a pH_2 flow rate of 60 scc/m at a pressure of 5 bar in a polarization field of 7 mT. (A) ^{1}H NMR signal (at 1 T) as a function of the buildup time at 7 mT. ^{1}H NMR signal (at 1 T) as a function of the waiting time (B) at the Earth's field and (C) at 7 mT. Bottom trace shows the same data as the top trace but with time axis presented on a logarithmic scale. The uneven distribution of points along the *x*-axis is caused by factoring in fluctuations in timing of the robotic arm recorded during the experiment.

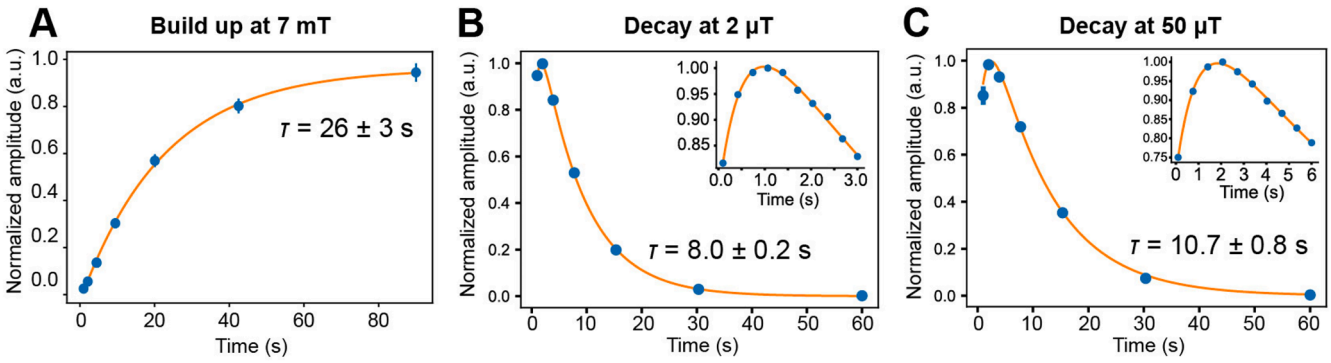

Fig. 5. Buildup and relaxometry curves of SABRE polarization in pyrazine (60 mM) with 5 mM [Ir(Imes)COD]Cl in methanol measured in the ultralow-field (ULF) regime (2 μT) using an optically pumped magnetometer. A) Buildup-curve of SABRE polarization, bubbling with parahydrogen at 5 bar, 30 scc/m in a field of 7 mT, fit with mono-exponential curve. B) Decay of SABRE polarization at 2 μT following 20 s of bubbling with all other parameters the same as in (A). The inset shows measurement of buildup of signal in the initial points of the curve. A bi-exponential function was used to fit the initial buildup seen in the curves. C) Decay of SABRE signal at Earth's field (~50 μT).

relaxometry experiments at 2 μT and at 50 μT, an interesting feature was observed: the signal shows an initial growth before expected decay. One of the likely explanations for the behavior observed in Fig. 5B-C is the fact that total proton signal is composed of both substrate and ortho-hydrogen proton signals but with opposite orientation with respect to the leading field. Relaxation time for the orthohydrogen is expected to be on the order of seconds while 7–10 s has been reported for non-degassed methanol [33]. The more surprising discrepancy of the time constants between the data obtained for the same polarization field of 7 mT but with different detection apparatuses (1 T benchtop NMR and ZULF NMR) may be attributed to contributions from different polarization transfer catalysts and/or spin orders. Another possible explanation is that even minor variations in the amounts of paramagnetic and catalyst-ligating impurities in the samples play a role. The efforts to explain SABRE observations with pyrazine are ongoing; the raw data for several benchtop and ULF experiments is provided as a repository on Zenodo.

3. Materials and methods

3.1. Automated Photo-CIDNP hyperpolarization

The sample was irradiated inside a 4-layer magnetic shield (Twinleaf, MS-2). The irradiation chamber was designed to accommodate NMR samples surrounded by up to 6 LEDs and a Hemholtz coil, and was printed out of acrylonitrile butadiene styrene using Ultimaker^2 Extended+ 3D printer. 4 LEDs (LED engine, LZ4-00G108-0000) with standard star MCPCB were used for irradiation. To avoid overheating, each of the LED was glued using epoxy glue (Loctite) to an aluminum heatsink (Ohmite, SV-LED-314E). Additionally, the temperature was stabilized using flow of dry air blown from below the sample to keep its temperature below 30 °C. Two sets of two LEDs connected in series were connected to the two outputs of a power supply (RS PRO bench power supply, 123-6467) through programmable relays (Mitsubishi, FX3S). Light intensity was controlled using the current output, the optimal value was found to be around 100 mA. This current corresponded to 0.2 W of the output light intensity per LED measured at 515 nm; approximately 0.1 W of light power from each LED reached the sample (distance of 5 mm). Light intensity was measured using an optical power meter from Thorlabs (PM100D).

The LEDs were connected to the power source using a twisted pair cable to minimize magnetic noise induced by current. The induced magnetic field was measured using fluxgate magnetometer (Bartington Instruments, Mag-01H). The LEDs themselves are slightly magnetic and even without any current were found to induce a residual field below 500 nT. Turning on the current increased the field; the measured field was <1 μT.

To provide the adiabatic change of magnetic field, the sample was transferred from the magnetic shield through a solenoid. The solenoid provided a magnetic field of 40 μT. Additionally, before sample transfer, the magnetic field around the sample was gradually increased using the Helmholtz coil. After this the field inside solenoid was turned on. The magnetic field-sweep was done linearly from 0 to 40 μT in 1 s, and was generated with an analogue output of Red Pitaya microcontroller that was further amplified (by AE tecron 7224) into linear sweep of current through the Helmholtz coil. These additional measures were not important for observation of the NMR lines corresponding to 2-^{13}C-BQ, these lines appeared anyway. However, the NMR lines corresponding to 1-^{13}C-BQ were not always observed without these measures.

In order to run hundreds of experiments and to have reproducible motion we used a robotic arm (Ufactory, Uarm Swift Pro). The arm took NMR samples using a "suction head"; it picked up each sample from the NMR spectrometer and dropped it there each time after the transfer from the shield to spectrometer. The motion from ZULF to the NMR spectrometer happened in 4.23 s. After the sample was placed inside the spectrometer a trigger signal was sent to start the acquisition. NMR spectra were acquired using Magritek Spinsolve 60 MHz spectrometer equipped with ^{13}C channel. The whole sequence of actions was programmed using a Python code, allowing synchronization of motion of the arm, LEDs state, magnetic fields in the coil and solenoid, and NMR acquisition.

3.2. Automated PHIP reactor valve control system

The SABRE experiments shown in Fig. 4 and Fig. 5 were performed by bubbling parahydrogen (>90 % enriched) at a pressure of 5 bar and flow rate of 30 sccm through a solution of 60 mM pyrazine and 5 mM [Ir(IMes)COD]Cl (IMes = 1,3-bis(2,4,6-trimethylphenyl) imidazole-2-ylidene, COD = cyclooctadiene) dissolved in methanol at 25 °C within a transfer field of 7 mT. To control the pH_2 bubbling time of experiments with greater precision and reproducibility, a system of three electrovalves (Swagelok, SS-BNS4-C/2O) linked to a central control unit was used. The control unit consisted of a microcontroller unit (MCU) (Arduino Uno) programmed to activate a series of mechanical relays (Tru Components, TC-9072496) to switch on/off power from a dedicated 24 V DC power supply (Mean Well, LRS-100–24). The power was sent by these relays to BNC connectors which the valves are connected to. Switching was controlled with Python (PyCharm, Community Edition) with pySerial and pyFirmata packages to allow communication between the MCU and computer. Bubbling time was controlled by either entering times manually within a given code or *via* a graphical user interface.

Pulse sequences were triggered automatically by sending a 5 V transistor-transistor logic (TTL) pulse from Arduino either: 1) directly to a benchtop NMR spectrometer (Magritek, Spinsolve Carbon 60 MHz) equipped with a dedicated port designed for this express purpose; 2) to an external MCU (Magritek, FTDI-UM232H) which relays a signal to a benchtop NMR spectrometer (Spinsolve Nitrogen Ultra 43 MHz) via USB connection to begin a pulse sequence. The second option includes an additional delay time of ~ 200 ms prior to activating a pulse sequence due to the secondary MCU.

In SABRE experiments, hydrogen is injected into the sample chamber using a 0.9 mm OD PTFE capillary that is inserted fully to the bottom of a 5 mm OD NMR tube inserted ~60 mm into a 4.8 mm inner-diameter, 6.4 mm outer-diameter PTFE tube. This is connected via a ¼" Swagelok nut and ferrule set to a T-connector attached to two 1/16" outer-diameter PTFE tubes which allow gas ingress and exhaust. These 1/16" tubes are connected to a valve board apparatus containing an array of three valves to control gas flow (see SI). The flow of hydrogen is controlled with a mass-flow controller (Sierra Instruments, SmartTrak 100) installed upstream of the reactor which produces stable flow rates from ~ 15 scc/min to 999.9 scc/min. The system pressure is maintained via a back-pressure regulator (Swagelok, KBP1G0A4A5A20000) and is typically set between 5 and 7 bar due to limitations presented by the glass NMR tubes used. See SI for additional details on this setup including materials and programming codes.

4. Conclusion and outlook

In this work, we demonstrate the use of an affordable benchtop NMR system in combination with an easily assembled robotic arm to conduct photo-CIDNP and SABRE benchtop hyperpolarization experiments. First, we show that robotization significantly enhances reproducibility of experiments. This is a sound advantage when greater accuracy is required, such as searches for weak signals using signal averaging. Therefore, automated systems seem promising in production environments, where consistency and repeatability are critical. In the context of hyperpolarization-enhanced NMR experiments, robotic systems are particularly advantageous for field cycling from high field to ZULF regime. This facilitates a wide range of experiments, including photo-CIDNP, DNP, PHIP/SABRE, two-dimensional NMR experiments, and relaxometry. Moreover, robotic arms help avoid complications, like those associated with fluidic systems including mixing-induced geometric and demagnetization field effects, which may lower observable signals. Apart from hyperpolarization, robotic systems also pair well with prepolarizing magnets, even when the magnetic fields used are not perfectly homogeneous. In summary, integration of robotic arms in hyperpolarization experiments offers clear advantages in terms of reproducibility, automation, and compatibility with a range of NMR field regimes, making them an attractive tool for advancing research in this area.

CRediT authorship contribution statement

Kirill Sheberstov: Writing – review & editing, Writing – original draft, Visualization, Validation, Software, Investigation, Conceptualization. **Erik Van Dyke:** Writing – review & editing, Writing – original draft, Visualization, Software, Methodology, Investigation, Formal analysis, Data curation. **Jingyan Xu:** Software, Methodology, Investigation. **Raphael Kircher:** Software, Methodology, Investigation. **Liubov Chuchkova:** Validation, Investigation, Formal analysis. **Yinan Hu:** Methodology, Investigation. **Sulaiman Alvi:** Methodology. **Dmitry Budker:** Writing – review & editing, Supervision, Resources, Funding acquisition, Data curation. **Danila A. Barskiy:** Writing – review & editing, Writing – original draft, Visualization, Supervision, Resources, Project administration, Methodology, Investigation, Funding acquisition, Data curation, Conceptualization.

Declaration of competing interest

The authors declare that they have no known competing financial interests or personal relationships that could have appeared to influence the work reported in this paper.

Acknowledgments

We gratefully acknowledge the financial support by the Alexander von Humboldt Foundation in the framework of the Sofja Kovalevskaja Award. KS acknowledges support by l'Agence Nationale de la Recherche (ANR) on the project ANR-24-CE93-0011-01.

Supplementary materials

Supplementary material associated with this article can be found, in the online version, at doi:10.1016/j.jmro.2025.100194.

Data availability

Raw data, Arduino and Python source codes, and the STL files for 3D printed parts are available at https://zenodo.org/records/14765446.

References

[1] J. Eills, D. Budker, S. Cavagnero, E.Y. Chekmenev, S.J. Elliott, S. Jannin, A. Lesage, J. Matysik, T. Meersmann, T. Prisner, J.A. Reimer, H. Yang, I.V. Koptyug, Spin hyperpolarization in modern magnetic resonance, Chem. Rev. 123 (2023) 1417–1551, https://doi.org/10.1021/acs.chemrev.2c00534.
[2] A. Abragam, M. Goldman, Principles of dynamic nuclear polarisation, Rep. Prog. Phys. 41 (1978) 395, https://doi.org/10.1088/0034-4885/41/3/002.
[3] J. Bargon, Joachim Bargon, Chance discoveries of hyperpolarization phenomena. Emagres, John Wiley & Sons, Ltd, 2010, https://doi.org/10.1002/9780470034590.emrhp1003.
[4] G.L. Closs, Mechanism explaining nuclear spin polarizations in radical combination reactions, J. Am. Chem. Soc. 91 (1969) 4552–4554, https://doi.org/10.1021/ja01044a043.
[5] R. Kaptein, J.L. Oosterhoff, Chemically induced dynamic nuclear polarization II: (Relation with anomalous ESR spectra), Chem. Phys. Lett. 4 (1969) 195–197, https://doi.org/10.1016/0009-2614(69)80098-9.
[6] H. Fischer, Chemically induced dynamic nuclear polarization: VI. Kinetic formulation of the radical pair mechanism, Z. Für Naturforschung A 25 (1970) 1957–1963, https://doi.org/10.1515/zna-1970-1227.
[7] P.F. Seidler, H.E. Bryndza, J.E. Frommer, L.S. Stuhl, R.G. Bergman, Synthesis of trinuclear alkylidyne complexes from dinuclear alkyne complexes and metal hydrides. CIDNP evidence for vinyl radical intermediates in the hydrogenolysis of these clusters, Organometallics 2 (1983) 1701–1705, https://doi.org/10.1021/om50005a045.
[8] J. Natterer, J. Bargon, Parahydrogen induced polarization, Prog. Nucl. Magn. Reson. Spectrosc. 31 (1997) 293–315, https://doi.org/10.1016/S0079-6565(97)00007-1.
[9] K. Laws, M. Tze-Kiat Ng, A. Sharma, Y. Jiang, A.J.S. Hammer, L. Cronin, An autonomous electrochemical discovery robot that utilises probabilistic algorithms: probing the redox behaviour of inorganic materials, ChemElectroChem 11 (2024) e202300532, https://doi.org/10.1002/celc.202300532.
[10] A. Sharma, M.T.-K. Ng, J.M. Parrilla Gutierrez, Y. Jiang, L. Cronin, A programmable hybrid digital chemical information processor based on the Belousov-Zhabotinsky reaction, Nat. Commun. 15 (2024) 1–10, https://doi.org/10.1038/s41467-024-45896-7.
[11] N.L. Bell, F. Boser, A. Bubliauskas, D.R. Willcox, V.S. Luna, L. Cronin, Autonomous execution of highly reactive chemical transformations in the Schlenkputer, Nat. Chem. Eng. 1 (2024) 180–189, https://doi.org/10.1038/s44286-023-00024-y.
[12] B.M. Matysiak, D. Thomas, L. Cronin, Reaction kinetics using a chemputable framework for data collection and analysis, Angew. Chem. Int. Ed. 63 (2024) e202315207, https://doi.org/10.1002/anie.202315207.
[13] P. Miéville, S. Jannin, G. Bodenhausen, Relaxometry of insensitive nuclei: optimizing dissolution dynamic nuclear polarization, J. Magn. Reson. 210 (2011) 137–140, https://doi.org/10.1016/j.jmr.2011.02.006.
[14] J. Yang, R. Xin, S. Lehmkuhl, J.G. Korvink, J.J. Brandner, Development of a fully automated workstation for conducting routine SABRE hyperpolarization, Sci. Rep. 14 (2024) 21022, https://doi.org/10.1038/s41598-024-71354-x.
[15] P. TomHon, E. Akeroyd, S. Lehmkuhl, E.Y. Chekmenev, T. Theis, Automated pneumatic shuttle for magnetic field cycling and parahydrogen hyperpolarized multidimensional NMR, J. Magn. Reson. 312 (2020) 106700, https://doi.org/10.1016/j.jmr.2020.106700.
[16] A.S. Kiryutin, V.P. Kozinenko, A.V. Yurkovskaya, Photo-SABRE: nuclear spin hyperpolarization of cis-trans photoswitchable molecules by parahydrogen,

ChemPhotoChem 8 (2024) e202300151, https://doi.org/10.1002/cptc.202300151.
[17] F. Ellermann, P. Saul, J.-B. Hövener, A.N. Pravdivtsev, Modern manufacturing enables magnetic field cycling experiments and parahydrogen-induced hyperpolarization with a benchtop NMR, Anal. Chem. 95 (2023) 6244–6252, https://doi.org/10.1021/acs.analchem.2c03682.
[18] C. Charlier, S.N. Khan, T. Marquardsen, P. Pelupessy, V. Reiss, D. Sakellariou, G. Bodenhausen, F. Engelke, F. Ferrage, Nanosecond time scale motions in proteins revealed by high-resolution NMR relaxometry, J. Am. Chem. Soc. 135 (2013) 18665–18672, https://doi.org/10.1021/ja409820g.
[19] A.S. Kiryutin, A.N. Pravdivtsev, K.L. Ivanov, Y.A. Grishin, H.-M. Vieth, A. V. Yurkovskaya, A fast field-cycling device for high-resolution NMR: design and application to spin relaxation and hyperpolarization experiments, J. Magn. Reson. 263 (2016) 79–91, https://doi.org/10.1016/j.jmr.2015.11.017.
[20] A.M.R. Hall, T.A.A. Cartlidge, G. Pileio, A temperature-controlled sample shuttle for field-cycling NMR, J. Magn. Reson. 317 (2020) 106778, https://doi.org/10.1016/j.jmr.2020.106778.
[21] T.B.R. Robertson, R.C. Bannister, T.A.A. Cartlidge, T. Hugger, S. Breham, K. Zick, F. Engelke, S. Thompson, G. Pileio, A dual-core NMR system for field-cycling singlet assisted diffusion NMR, Front. Chem. 11 (2023), https://doi.org/10.3389/fchem.2023.1229586.
[22] R.E. Mewis, K.D. Atkinson, M.J. Cowley, S.B. Duckett, G.G.R. Green, R.A. Green, L. A.R. Highton, D. Kilgour, L.S. Lloyd, J.A.B. Lohman, D.C. Williamson, Probing signal amplification by reversible exchange using an NMR flow system, Magn. Reson. Chem. 52 (2014) 358–369, https://doi.org/10.1002/mrc.4073.
[23] P.M. Richardson, A.J. Parrott, O. Semenova, A. Nordon, S.B. Duckett, M.E. Halse, SABRE hyperpolarization enables high-sensitivity 1H and 13C benchtop NMR spectroscopy, Analyst 143 (2018) 3442–3450, https://doi.org/10.1039/C8AN00596F.
[24] K. Kouřil, H. Kouřilová, S. Bartram, M.H. Levitt, B. Meier, Scalable dissolution-dynamic nuclear polarization with rapid transfer of a polarized solid, Nat. Commun. 10 (2019) 1733, https://doi.org/10.1038/s41467-019-09726-5.
[25] J.A. Villanueva-Garibay, A. Tilch, A.P. Aguilar Alva, G. Bouvignies, F. Engelke, F. Ferrage, A. Glémot, U.B. le Paige, G. Licciardi, C. Luchinat, G. Parigi, P. Pelupessy, E. Ravera, A. Ruda, L. Siemons, O. Stenström, J.-M. Tyburn, A fast sample shuttle to couple high and low magnetic fields. Applications to high-resolution relaxometry, Magn. Reson. Discuss. (2025) 1–23, https://doi.org/10.5194/mr-2024-25.
[26] R.W. Adams, J.A. Aguilar, K.D. Atkinson, M.J. Cowley, P.I.P. Elliott, S.B. Duckett, G.G.R. Green, I.G. Khazal, J. López-Serrano, D.C. Williamson, Reversible interactions with para-hydrogen enhance NMR sensitivity by polarization transfer, Science 323 (2009) 1708–1711, https://doi.org/10.1126/science.1168877.
[27] K.F. Sheberstov, L. Chuchkova, Y. Hu, I.V. Zhukov, A.S. Kiryutin, A.V. Eshtukov, D. A. Cheshkov, D.A. Barskiy, J.W. Blanchard, D. Budker, K.L. Ivanov, A. V. Yurkovskaya, Photochemically induced dynamic nuclear polarization of heteronuclear singlet order, J. Phys. Chem. Lett. 12 (2021) 4686–4691, https://doi.org/10.1021/acs.jpclett.1c00503.
[28] E.T. Van Dyke, J. Eills, R. Picazo-Frutos, K.F. Sheberstov, Y. Hu, D. Budker, D. A. Barskiy, Relayed hyperpolarization for zero-field nuclear magnetic resonance, Sci. Adv. 8 (2022) eabp9242, https://doi.org/10.1126/sciadv.abp9242.
[29] L. Chuchkova, S. Bodenstedt, R. Picazo-Frutos, J. Eills, O. Tretiak, Y. Hu, D. A. Barskiy, J. de Santis, M.C.D. Tayler, D. Budker, K.F. Sheberstov, Magnetometer-detected nuclear magnetic resonance of photochemically hyperpolarized molecules, J. Phys. Chem. Lett. 14 (2023) 6814–6822, https://doi.org/10.1021/acs.jpclett.3c01310.
[30] S. Alcicek, P. Put, V. Kontul, S. Pustelny, Zero-field NMR J-spectroscopy of organophosphorus compounds, J. Phys. Chem. Lett. 12 (2021) 787–792, https://doi.org/10.1021/acs.jpclett.0c03532.
[31] S. Alcicek, E. Van Dyke, J. Xu, S. Pustelny, D.A. Barskiy, 13C and 15N benchtop NMR detection of metabolites via relayed hyperpolarization, Chem. Methods 3 (2023) e202200075, https://doi.org/10.1002/cmtd.202200075.
[32] G.R. Stadler, T.F. Segawa, M. Bütikofer, V. Decker, S. Loss, B. Czarniecki, F. Torres, R. Riek, Fragment screening and fast micromolar detection on a benchtop NMR spectrometer boosted by photoinduced hyperpolarization, Angew. Chem. Int. Ed. 62 (2023) e202308692, https://doi.org/10.1002/anie.202308692.
[33] H. Zeng, J. Xu, J. Gillen, M.T. McMahon, D. Artemov, J.-M. Tyburn, J.A.B. Lohman, R.E. Mewis, K.D. Atkinson, G.G.R. Green, S.B. Duckett, P.C.M. van Zijl, Optimization of SABRE for polarization of the tuberculosis drugs pyrazinamide and isoniazid, J. Magn. Reson. 237 (2013) 73–78, https://doi.org/10.1016/j.jmr.2013.09.012.